Showcasing research from Professor Chi Zhang's laboratory, School of Chemical Science and Engineering, Tongji University, Shanghai, China.

Greatly enhanced ultrafast optical absorption nonlinearities of pyridyl perovskite nanocrystals axially modified by star-shaped porphyrins

This image highlights a pyridyl $CsPbBr_3$ perovskite nanocrystal with a regular lattice structure in the center of dark-blue background. Its terminal light-blue N atom forms a unique axial coordination interaction with the light-red Zn atom of the star-shaped porphyrin located in the upper left and lower parts of the image. The two communicate with each other in the perovskite-porphyrin binary system through purple comet-shaped ribbons, optimizing the nonlinear optical absorption properties of the hybrid material. The ultrashort laser irradiates the sample, vividly demonstrating the light-matter interaction between laser and nanocrystal.

Image reproduced by Chi Zhang et al. from Chem. Sci., 2025, **16**, 6720.

As featured in:

See Chi Zhang et al.,
Chem. Sci., 2025, **16**, 6720.

ROYAL SOCIETY
OF CHEMISTRY

15 YEARS
ANNIVERSARY

rsc.li/chemical-science

EDGE ARTICLE

Check for updates

Greatly enhanced ultrafast optical absorption nonlinearities of pyridyl perovskite nanocrystals axially modified by star-shaped porphyrins†

Zihao Guan,‡[a] Lulu Fu,‡[a] Lu Chen, [ID][a] Zhiyuan Wei,[a] Fang Liu,[a] Yang Zhao,[a] Zhipeng Huang, [ID][a] Mark G. Humphrey [ID][b] and Chi Zhang [ID] *[a]

The long-chain ligands and weak charge-transport capacity of perovskite nanocrystals (NCs) always hinder their optoelectronic applications. Our study proposes an effective strategy to unlock the optimized nonlinear optical (NLO) properties of perovskite *via* aromatic ligand-exchange plus porphyrin-axial-coordination. The synthesized porphyrin–pyridine dual-modified CsPbBr₃-NC hybrid material, fabricated using 4-(aminomethyl)pyridine (PyMA) and a novel star-shaped zinc-porphyrin trisubstituted triazacoronene compound (ZnPr), exhibits excellent NLO absorption performance under femtosecond (fs) laser irradiation in the visible to near-infrared range. Specifically, its nonlinear absorption coefficient is 10 times higher than that of the pristine CsPbBr₃-NC and it also possesses an outstanding optical limiting (OL) capability with an OL threshold as low as 1.8 mJ cm⁻². The modification of PyMA ligands reduces the trap state density on the perovskite surface and promotes the electronic coupling between the NC lattices. With the aid of PyMA coordinating with the Zn atoms in ZnPr, large-size planar porphyrins are anchored on the perovskite surface from the axial position, which may enhance the ligand protection capability and thereby significantly facilitate the charge transport between porphyrin components and perovskite NCs. The above two-step modification synergistically contributes to the prominent NLO performance. Our work affords a new viable paradigm for developing multi-field and high-performance perovskite NC photonic materials and devices.

1 Introduction

All-inorganic halide perovskite nanocrystals (NCs), due to their long carrier lifetime,[1] easy-to-tune bandgap,[2,3] efficient carrier mobility,[4] high fluorescence quantum yield,[5,6] low-cost fabrication,[7] and the possibility of solution-based processing,[8] are attracting increasing attention for their practical applications in advanced optoelectronic technologies. Since cesium halide perovskite NCs (CsPbX₃, X = Cl, Br, I) were reported in 2015,[9] optoelectronic devices based on them have been comprehensively developed, such as light-emitting diodes,[10,11] solar cells,[12] photodetectors,[13,14] fluorescence imaging,[15] lasers,[16,17] *etc.* Recently, perovskite nanocrystal (NC) materials have become a hot topic in next-generation optoelectronics research due to their nanoscale characteristics showing inherent surface-rich properties[18] and

quantum confinement effects.[19,20] In particular, it becomes possible to develop nonlinear optical (NLO) materials based on perovskite NCs.[21] In contrast to the three-dimensional perovskite, although the stability of perovskite NCs is greatly improved, there are still many defect sites on their surfaces, such as vacancies or dangling bonds,[22] which considerably weaken the optical properties. Most methods for preparing perovskite NCs nowadays utilize oleylamine and oleic acid as surface ligands,[23,24] which can passivate perovskite defects by establishing robust coordination bonds with the NC surface. However, these long-chain ligands are electrically insulated and present energy barriers, impeding the carrier transport inside the perovskite NCs.[25,26] In addition, long molecular chains lead to the excessive distance between individual nanocrystal particles that also reduces the carrier mobility and affects the charge transport between perovskite NCs,[27] which is unfavorable for photonic device development. Therefore, the design and preparation of perovskite NCs with sufficient light absorption capability and excellent charge-transporting performance is a crucial challenge for developing high-performance perovskite-based NLO materials.

To address such problems, various studies have been dedicated to the modification of ligands on the perovskite NC surface. Among them, "ligand exchange" has been employed many times in conventional quantum dot preparation.[28–30] The

[a]*China-Australia Joint Research Center for Functional Molecular Materials, School of Chemical Science and Engineering, Tongji University, Shanghai 200092, China. E-mail: chizhang@tongji.edu.cn*

[b]*Research School of Chemistry, Australian National University, Canberra, ACT 2601, Australia*

† Electronic supplementary information (ESI) available: Experimental section and characterization data. See DOI: https://doi.org/10.1039/d4sc08175g

‡ These authors contributed equally.

main focus of enhancing the charge transport and interdot electronic coupling properties of perovskite NCs lies in rationally tuning the surface ligand length.[31,32] For example, Park *et al.* systematically investigated and found that short alkyl chain ligands with small volumes have a higher surface passivation effect and less aggregation, promoting the carrier transport capability and realizing more efficient optoelectronic performance.[33] Nevertheless, it does not alter the essence of ligand electrical insulation. The charge transport dilemma between perovskite NCs is still an important factor limiting their photonic performance. Potential ligands with hydrophobicity and conductivity are not exclusively limited to aliphatic compounds, as alkenes, alkynes, and aromatic compounds also have unhindered positive and negative terminal ions that can interact with perovskite components. Especially aromatic compounds, with their π–electron resonance delocalization characteristics, combined with their own stability and adjustable electronic structure, hold promising prospects for applications in the realm of optoelectronics. More importantly, they may significantly change the insulation disadvantage of aliphatic compounds. The π–electron delocalization allows them to serve as an effective medium for facilitating charge transport between perovskite inorganic octahedral lattices.[34,35]

Porphyrins, with the π–π* transition of their conjugated macrocycles and high molar extinction coefficients, exhibit strong light absorption.[36] Their photoelectric properties can be tailored by varying functional groups, making them very promising NLO materials.[37–40] Studies have demonstrated that some organic ligands can form axial coordination with the central metal atom of the porphyrin macrocycle,[41] thereby communicating the charge transport pathway between the two components: the porphyrin and the organic ligand. For example, Batista *et al.* employed pyridine-containing isonicotinic acid as a connecting bridge to axially interact with the central metal ion of the photosensitizer porphyrin, thereby constructing an electron transport route from the solar-excited dye molecule to the semiconductor host substrate and successfully developing a high-performance dye-sensitized solar cell.[42] Inspired by these studies, the effective utilization of axial coordination characteristics of porphyrins, the rational design of aromatic compound ligands and porphyrin molecules, and introducing them into the perovskite NC systems are expected to construct new perovskite NC hybrid materials that can exhibit desirable performance in the NLO field.

Herein, a novel and effective strategy to boost the nonlinear absorption performance through perovskite NC surface engineering, specifically *via* aromatic ligand-exchange plus porphyrin-axial-coordination, was proposed. We used 4-(aminomethyl)pyridine (PyMA) as the surface ligand, which also functions as the axial coordination group, to partially replace the oleylamine ligand for modifying perovskite NCs. A series of PyMA-modified $CsPbBr_3$ perovskite NCs ($PyMA-CsPbBr_3$-NCs) with different PyMA contents were synthesized. A novel star-shaped zinc porphyrin trisubstituted triazacoronene compound (ZnPr) was then designed and introduced into the above modified perovskite NCs. Through axially combining the transition metal Zn in ZnPr with the pyridine group of the PyMA

surface ligand on perovskite, the porphyrin–pyridine dual-modified perovskite NC hybrid material ($ZnPr-PyMA-CsPbBr_3$-NC) was successfully constructed. Z-scan tests show that both $PyMA-CsPbBr_3$-NCs and $ZnPr-PyMA-CsPbBr_3$-NC exhibited significantly enhanced NLO absorption properties under 800 and 515 nm femtosecond (fs) lasers excitation. The ZnPr-PyMA-$CsPbBr_3$-NC displayed an excellent optical limiting (OL) threshold of 1.8 mJ cm^{-2} at 800 nm, lower than that of most reported OL materials. The above-mentioned excellent NLO responses can be attributed to the passivation of the perovskite defect sites and stabilization of the perovskite NC structure *via* the introduction of the PyMA surface ligand. Its aromatic structure can promote the ligand regular arrangement, improve the electrical conductivity, and strengthen the electronic coupling between NCs. The strong axial coordination interaction of pyridine-metal connects the PyMA ligand on the NC surface and ZnPr, which improves ligand protective ability and suppresses non-radiative loss. The photo-generated excitons are firmly bound within perovskite NC lattices and interact with the photoelectric field to generate a large exciton binding energy. Most importantly, the axial coordination interaction opens up important charge transport channels among porphyrin molecules, surface ligands, and perovskite lattices, promoting charge transport while avoiding non-radiative loss. Various factors synergistically facilitate the superb NLO performance of the $ZnPr-PyMA-CsPbBr_3$-NC hybrid material. Our work demonstrates that introducing functional ligands and highly photo-active components into perovskite NCs *via* ligand exchange plus axial coordination interaction is an effective solution to optimize the NLO properties of perovskite NCs. The as-prepared multi-component nanohybrid materials provide a new paradigm and an experience for the further development of multi-functional and highly sensitive NLO devices.

2 Experimental details

2.1. Materials

$PbBr_2$ (99%, RG) and Cs_2CO_3 (99%, RG) were purchased from Aladdin Reagent. Oleylamine (90%+, RG), oleic acid (99%, RG), 1-octadecene (90%, RG), *n*-hexane (97%, RG), and methyl acetate (98%, RG) were obtained from Sinopharm Chemical Reagent. 4-(Aminomethyl)pyridine (PyMA, 98%, RG), polymethyl methacrylate (PMMA, transmittance 92%, RG), and other chemicals were purchased from Titan Technologies Inc. The star-shaped zinc porphyrin trisubstituted triazacoronene compound (ZnPr) was successfully synthesized *via* Ullmann coupling, reduction, amidation, Bischler–Napieralski cyclization, and Suzuki–Miyaura coupling reactions from dipyrromethane and 2,3-dichloronitrobenzene compounds, as presented in Scheme S1.† The characterization of ZnPr and intermediates was performed by NMR and MALDI-TOF techniques.[43]

2.2. Measurements and characterization studies

The morphology of the samples was characterized using high-resolution transmission electron microscopy (TEM) with the

instrument model JEMF200. The molecular weights were determined by matrix-assisted laser desorption ionization time-of-flight mass spectrometry (MALDI-TOF), and the instrument model was Bruker Autoflex III. ^{1}H and ^{13}C NMR spectra were measured with a Bruker AV 600 Hz nuclear magnetic resonance spectrometer (NMR) at a test temperature of 15 °C using tetramethylsilane as a chemical shift internal standard. X-ray diffraction (XRD) patterns were recorded using a Rigaku Ultima IV X-ray powder diffractometer, and the radiation source was Cu Kα ($\lambda = 1.54$ Å). X-ray photoelectron spectra (XPS) were obtained using an X-ray photoelectron spectrometer (AXIS Ultra DLD) with an Al Kα X-ray source, and based on the calibration data of the C 1s element with a binding energy of 284.8 eV. An Agilent Cary 5000 ultraviolet-visible spectroscopy (UV-vis) instrument was employed to record absorption spectra of the samples. Steady-state photoluminescence (PL), photoluminescence quantum yield (PLQY), and time-resolved photoluminescence (TRPL) spectra of the samples were recorded using a Horiba Fluorolog-3 transient fluorescence spectrometer. Fourier transform infrared spectra (FT-IR) of the samples were recorded using a Thermo Scientific Nicolet iS20 infrared spectrometer. Other characterization methods are provided in the ESI.†

2.3. Preparation of PyMA-CsPbBr₃-NCs

2.3.1. Synthesis of cesium oleate. Cs$_2$CO$_3$ (162.8 mg), oleic acid (1.6 mL), and 1-octadecene (8 mL) were added to a two-neck flask. The mixture was stirred and heated to 120 °C and vacuum-dried for 1 h. Then, it was heated to 150 °C under an N$_2$ atmosphere until the solution appeared transparent and was kept aside for further use.

2.3.2. Synthesis of CsPbBr₃ perovskite NCs. A mixture of PbBr$_2$ (0.2 g), oleic acid (1.5 mL), 1-octadecene (15 mL), and oleylamine (3 mL) was added into a two-neck flask, and then repeatedly filled and released N$_2$ three times. The mixture was heated to 120 °C and stirred while degassing with a vacuum pump for 30 min. After completion, the mixed solution was heated to 170 °C and stirred for 10 min under a N$_2$ atmosphere. When the solution became transparent, the cesium oleate solution (1.2 mL) at 150 °C was quickly drawn into a glass syringe and immediately injected into the mixed solution in the two-necked flask. After 5 s, the two-necked flask was quickly placed in an ice bath to cool down, and it was continuously shaken until the solution turned bright yellow-green. After the reaction was completed, methyl acetate (50 mL) was added to the crude mixed solution, and centrifuged at 8000 rpm for 5 min; then the supernatant was removed, and the precipitate was dispersed again in n-hexane/methyl acetate (1 : 1, v/v) and centrifuged at 8000 rpm for 2 min. Then the supernatant was removed again, the precipitate was dispersed in n-hexane (5 mL) again and centrifuged at 4000 rpm for 5 min. The supernatant was removed, and ultimately, the precipitate was dispersed in a toluene solution for subsequent testing.

2.3.3. Synthesis of PyMA-CsPbBr₃-NCs. The synthesis method follows the synthesis steps of CsPbBr$_3$ perovskite NCs. For different PyMA-modified CsPbBr$_3$ NCs, except for the unchanged addition amounts of PbBr$_2$, oleic acid, and 1-octadecene, 3 mL of oleylamine was partially substituted with PyMA in varying mass fractions from 0.075 to 0.25 and added into the flask.

2.3.4. Preparation of ZnPr-PyMA-CsPbBr₃-NCs. 6 mL of 0.5 mg per mL PyMA-CsPbBr$_3$-NC toluene solution was taken and N$_2$ was bubbled through it for 1 h to remove dissolved oxygen. Then, 10^{-4} M ZnPr porphyrin molecules were added to the solution, and the mixture was stirred and reacted for 2 h to obtain ZnPr-PyMA-CsPbBr$_3$-NCs. N$_2$ was bubbled through the solution for another 10 min and it was left to stand for further characterization.

As a comparative experiment, the porphyrin-CsPbBr$_3$ perovskite NCs (ZnPr-CsPbBr$_3$-NC) were also prepared. The preparation procedures were the same as the above methods, and the initial solution was 6 mL of 0.5 mg per mL CsPbBr$_3$-NC toluene solution.

2.4. Preparation of perovskite NC films

PMMA particles (1.5 g) were added to the prepared perovskite NCs toluene solution (6 mL). The mixture was placed on a heating platform at 50 °C and stirred until the PMMA particles were completely dissolved and the solution appeared viscous and transparent. Then, the solution was poured into a glass Petri dish with a diameter of 10 cm, and the Petri dish was gently shaken until no bubbles were generated in the solution. Subsequently, the Petri dish was placed in a vacuum-drying oven at 45 °C to dry for approximately 48 h. The light-transmitting and smooth perovskite NC PMMA films were obtained and was kept aside for further characterization tests. The concentration of all samples in the PMMA matrix was determined to be 2.4 mg mL^{-1}.

2.5. NLO measurements

The NLO absorption properties of perovskite NC samples were measured at 800 and 515 nm using an fs Ti:sapphire regenerative amplified laser (Spitfire ACE-35F-2KXP, Spectra-Physics). The laser pulse duration was 34 fs with a repetition rate of 1 kHz. The sample was positioned on the Z-scan optical path, and the Z-axis movement ($-Z$ to $+Z$) was controlled by the computer. The functional relationship between different nonlinear transmittances and position Z was recorded by measuring the ratio of transmitted fluence to input fluence. The Z-scan curves obtained can be fitted to calculate the β values through the following equations:[44]

$$T(Z) = \sum_{m=0}^{\infty} \frac{[-q_0(Z)]^m}{(m+1)^{3/2}} \tag{1}$$

$$q_0(Z) = \frac{\beta I_0 L_{\text{eff}}}{\left(1 + \dfrac{Z^2}{Z_0{}^2}\right)} \tag{2}$$

$$L_{\text{eff}} = \frac{1 - e^{-\alpha_0 L}}{\alpha_0} \tag{3}$$

where $T(Z)$ is the normalized transmittance; Z is the sample propagation distance; α_0 is the linear absorption coefficient; β is

the nonlinear absorption coefficient; L is the measured sample thickness; and Z_0 is the diffraction length of a laser beam. Additionally, the calculation instructions for excited state absorption (σ_e) and ground state absorption (σ_g) cross sections in SA are provided in the ESI.†

3   Results and discussion

3.1.   Construction of the porphyrin-pyridyl perovskite NC hybrid material

A series of perovskite NC materials were prepared by the hot-injection method. The unmodified pristine $CsPbBr_3$-NC was obtained by adding a mixture of oleic acid and oleylamine to 1-octadecene and reacting rapidly at a high temperature of 170 °C with the participation of cesium oleate and $PbBr_2$, as shown in Fig. 1a. For pyridyl perovskite NCs, added oleylamine was partially replaced by the 4-(aminomethyl)pyridine surface ligand to obtain pyridyl perovskite NCs with different ratios, which was marked as "0.075 PyMA-$CsPbBr_3$-NC", "0.15 PyMA-$CsPbBr_3$-NC", and "0.25 PyMA-$CsPbBr_3$-NC". Through repeated dispersion and centrifugation of methyl acetate and n-hexane, excess surface ligands and impurities were removed. The finally obtained precipitate was redissolved and dispersed in toluene to obtain a uniformly dispersed colloidal solution of pyridyl perovskite NCs, which was used for further characterization.

Porphyrin trisubstituted triazacoronene organic compound ZnPr exhibits excellent NLO performance. Fig. 1c and S1–S3† show its chemical structure, nuclear magnetic resonance (NMR) spectra, and matrix-assisted laser desorption ionization time-of-flight mass spectrometry (MALDI-TOF) diagrams, confirming the authenticity of the ZnPr structure. Its strongly hydrophobic and cyclic π-conjugated structure is expected to protect the perovskite surface from the external environment. More importantly, ZnPr features a zinc porphyrin component with three substitutions, and the pyridine group of the PyMA ligand in perovskite NCs can form the axial coordination interaction with the metal zinc ion in the porphyrin center (Fig. 1c). Therefore, on the basis of the prepared pyridyl perovskite NCs, a freshly prepared toluene solution of ZnPr was introduced into the dispersed colloidal solution of pyridyl perovskite NCs. The mixture was stirred for 2 h to attain a uniform and stable state, and the porphyrin-modified pyridyl perovskite NC hybrid material was obtained, as shown in Fig. 1a, which can be labeled as "ZnPr-PyMA-$CsPbBr_3$-NC". In order to better evaluate the special axial coordination interaction of pyridyl perovskite NCs to ZnPr, a toluene solution with the same molar mass of ZnPr was also prepared and added to the original $CsPbBr_3$-NC solution. Other conditions remained unchanged, and this mixed solution is labeled as "ZnPr-$CsPbBr_3$-NC" as a reference control group. Additionally, the above colloidal solutions were
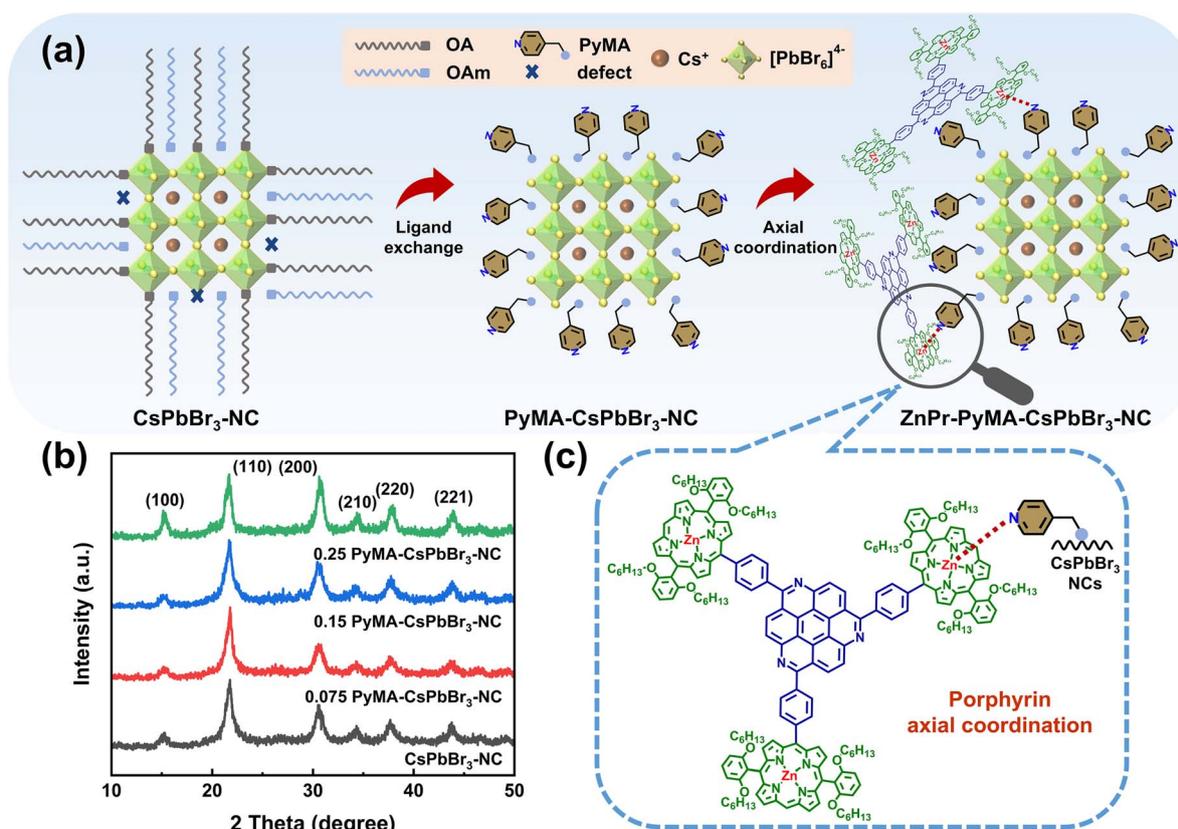

Fig. 1 (a) Schematic diagram for the preparation process of the pristine, PyMA-modified, and ZnPr–PyMA-modified $CsPbBr_3$ perovskite NCs and their corresponding detailed structures (including the interaction of porphyrin, PyMA ligand, and perovskite NC). (b) XRD patterns of the pristine and modified $CsPbBr_3$ NCs with different PyMA contents. (c) The magnified schematic diagram of the molecular structure of ZnPr and its axial interaction with the PyMA ligand.

also prepared into PMMA films, and NLO properties of these perovskite NC films were investigated.

3.2. Structural characterization of pyridyl perovskite NCs

The pyridyl perovskite NCs with different PyMA contents were detected using an X-ray diffractometer (XRD), and the corresponding XRD patterns are shown in Fig. 1b. All samples exhibited three distinct XRD diffraction peaks at 15.1°, 21.7°, and 30.7°, which correspond to the (100), (110), and (200) crystal planes of the perovskite cubic structure, respectively.[27] Other weaker XRD diffraction peaks also reveal the lattice structure characteristics of perovskite NCs.[45] Upon the introduction of PyMA ligands, their cubic structure remains intact without being disturbed, manifesting that PyMA, with less steric hindrance, exerts a slight influence on the crystal structure of perovskite NCs during the synthesis process.[46]

The morphology of the prepared perovskite NCs was further explored using high-resolution transmission electron microscopy (TEM), as shown in Fig. 2a–d. The pristine and PyMA-treated CsPbBr$_3$ NCs consist of square grains that are tightly arranged on the copper mesh. Fig. 2e–h show high-resolution TEM images of the corresponding samples. Regardless of whether PyMA was added or the amount of PyMA added, all perovskite NCs retained a complete orthorhombic crystal structure and cubic morphology. The lattice fringes with a spacing of 0.58 nm correspond to the (110) crystal plane of the CsPbBr$_3$ NC orthorhombic phase.[47] This is consistent with the results reflected in XRD spectra, indicating that the introduction of PyMA ligands does not disrupt the inherent crystal structure of perovskite NCs. The cubic sizes of PyMA-CsPbBr$_3$-NCs increase gradually with the PyMA addition and increase of PyMA content. Particle size statistics were performed on the above TEM images to generate particle size distribution histograms, as depicted in Fig. 2i–l. The cubic size of the pristine CsPbBr$_3$-NC is 10.9 nm, while those of 0.075 PyMA-CsPbBr$_3$-NC, 0.15 PyMA-CsPbBr$_3$-NC, and 0.25 PyMA-CsPbBr$_3$-NC are 14.5, 15.4, and 17.3 nm, respectively. Since the molecular structure of PyMA is smaller than that of long-chain oleylamine molecules, PyMA presents less steric hindrance than oleylamine. Consequently, when PyMA coordinates to the perovskite lattice surface, it can evidently promote the growth of larger-sized NCs.[27] The above results demonstrate that the PyMA ligand introduction has a significant impact on the nucleation and growth kinetics of NCs during the synthesis process. Among them, the 0.25 PyMA-CsPbBr$_3$-NC possesses better surface morphology and lattice structure, so it is expected to possess greater potential in terms of optoelectronic properties, which still needs further verification.

3.3. Photophysical properties of pyridyl perovskite NCs

Ultraviolet-visible (UV-vis) and steady-state photoluminescence (PL) spectroscopy were employed to investigate the photophysical properties of pyridyl perovskite NCs through the uniform dispersion of an equal amount of perovskite NCs in
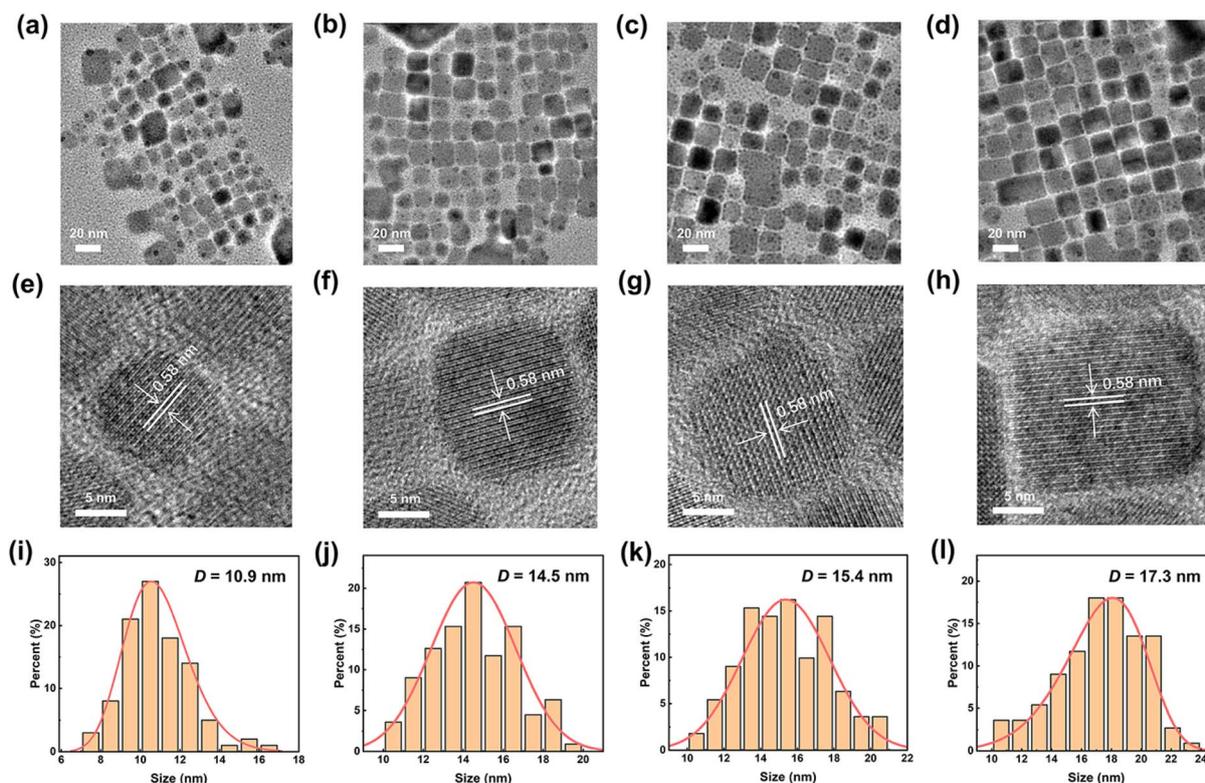

Fig. 2 (a)–(d) TEM images, (e)–(h) high-resolution TEM images, and (i)–(l) corresponding particle size distribution diagrams for the pristine CsPbBr$_3$-NC and 0.075, 0.15, and 0.25 PyMA-CsPbBr$_3$-NCs. D is the average particle size.

toluene. Fig. 3a presents the UV-vis spectra of CsPbBr₃ NCs without and with different contents of PyMA treatment. The results showed that their UV-vis curves did not exhibit significant changes, and the characteristic peaks were located at 490, 493, 492, and 504 nm, respectively. Compared with the pristine CsPbBr₃-NC, the absorption edges of PyMA-modified perovskite NCs were red-shifted, indicating an enhancement in their visible light absorption capacities. Additional absorption peaks at 389 and 431 nm were detected for the 0.25 PyMA-CsPbBr₃-NC, which may be ascribed to the higher excited state absorption of NCs induced by excess organic ligands.[48] Fig. 3b shows that all perovskite NCs appear bright yellow-green under natural light. Fig. 3d displays their corresponding fluorescence emission spectra. As the content of PyMA increased from 0 to 0.25, the characteristic emission peaks of CsPbBr₃ NCs before and after modification red-shifted from 508 to 515 nm, accompanied by an increase in fluorescence intensity. This may be attributed to the larger particle size of PyMA-CsPbBr₃-NCs. The resulting quantum confinement effect is weakened, leading to a shift in the fluorescence emission peak towards longer wavelengths. The fluorescence decay curves of CsPbBr₃ NCs before and after PyMA modification were measured *via* time-resolved photoluminescence (TRPL) spectroscopy to evaluate their photogenerated carrier lifetime. Fig. 4 gives the decay curves for the pristine CsPbBr₃-NC, 0.075 PyMA-CsPbBr₃-NC, 0.15 PyMA-CsPbBr₃-NC, and 0.25 PyMA-CsPbBr₃-NC, fitted with a double exponential function to obtain the τ_1 and τ_2 lifetime values for the corresponding materials, as follows:

$$y_0 = B + A_1 e^{-\frac{t}{\tau_1}} + A_2 e^{-\frac{t}{\tau_2}} \tag{4}$$

where B is a constant for the background offset, y is the emission intensity, and A_1 and A_2 are fluorescence decay amplitudes. The fluorescence decay lifetime mainly includes two components: short (τ_1) and long lifetime (τ_2), which are respectively derived from the recombination process related to trap state capture and the recombination process of intrinsic radiation
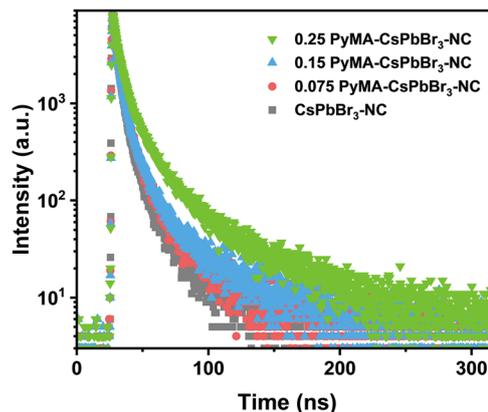

Fig. 4 TRPL decay curves for the pristine CsPbBr₃-NC and PyMA-modified CsPbBr₃ NCs.

excitons.[47,49] After fitting calculation, the τ_1 and τ_2 for CsPbBr₃-NC, 0.075 PyMA-CsPbBr₃-NC, 0.15 PyMA-CsPbBr₃-NC, and 0.25 PyMA-CsPbBr₃-NC are 2.4 and 8.8 ns, 2.5 and 10.1 ns, 2.9 and 12.2 ns, and 3.8 and 17.6 ns, respectively. Compared with the pristine CsPbBr₃-NC, the PyMA-CsPbBr₃-NCs exhibited slower fluorescence decay and a longer lifetime. Moreover, increasing the PyMA content enhances the crystal size of NCs, which weakens the quantum confinement effect and thus leads to longer lifetimes.[50] The photoluminescence quantum yield (PLQY) values of PyMA-modified perovskite NCs have also been measured and are shown in Fig. S4.† As the PyMA content increases, their PLQY values show an upward trend, reaching a maximum value (84%) when the content is 0.25, which is consistent with the longer lifetime tested by TRPL. These results indicate that PyMA ligand introduction enables NCs with less steric hindrance in comparison to long-chain oleylamine ligands, resulting in greater degrees of freedom and flexibility. PyMA can passivate defects that long-chain oleylamine cannot reach, thus effectively reducing the trap state density and
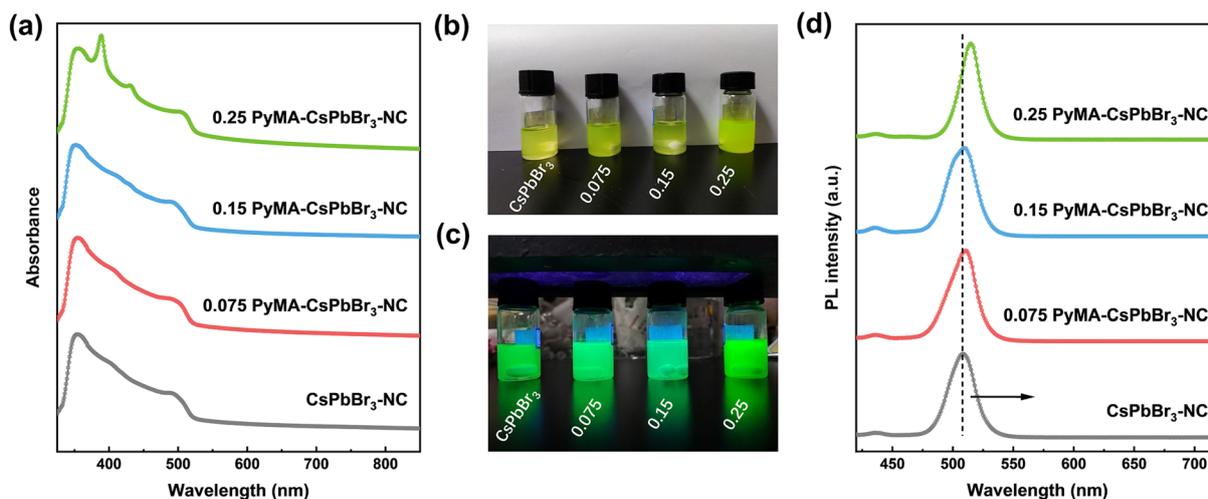

Fig. 3 (a) UV-vis spectra, images under (b) natural light and (c) 365 nm UV lamp, and (d) emission spectra for CsPbBr₃ NCs without and with different contents of PyMA treatment.

inhibiting the non-radiative recombination in perovskite NCs. It is worth noting that all four materials exhibit strong green fluorescence under UV light irradiation, as shown in Fig. 3c. The fluorescence of the 0.25 PyMA-CsPbBr$_3$-NC is the strongest, also consistent with the results observed in the above fluorescence spectra, corresponding lifetime curves and PLQY values. To sum up, the 0.25 PyMA-CsPbBr$_3$-NC has the best morphology, structure, and photophysical properties, and is anticipated to exhibit excellent NLO performance. Therefore, the following characterization and performance testing were performed utilizing the optimized 0.25 PyMA-CsPbBr$_3$-NC.

3.4. Surface ligand characterization of pyridyl perovskite NCs

While the aforementioned characterization studies suggest the successful preparation of PyMA-CsPbBr$_3$-NCs, there is still a lack of sufficient evidence to prove whether PyMA acts as a surface ligand that is anchored on the perovskite NC surface. Therefore, the prepared samples were tested using the Fourier transform infrared spectroscopy (FT-IR) technique to explore the variations of ligands on the surface of perovskite NCs. Fig. 5 shows FT-IR spectra of the PyMA monomer, CsPbBr$_3$-NC, and 0.25 PyMA-CsPbBr$_3$-NC, along with extended spectra of several important parts. As displayed in Fig. 5a, the FT-IR peaks at 2853, 2922, and 1465 cm^{-1} can be observed in the CsPbBr$_3$-NC and 0.25 PyMA-CsPbBr$_3$-NC, corresponding to –CH$_2$ asymmetric stretching vibration, symmetrical stretching vibration, and bending vibration, which are derived from the alkyl chains of oleylamine and oleic acid. Owing to the presence of oleylamine

and oleic acid ligands in both the CsPbBr$_3$-NC and 0.25 PyMA-CsPbBr$_3$-NC, the same FT-IR characteristic peaks can be observed. However, in the 0.25 PyMA-CsPbBr$_3$-NC, the intensities of these FT-IR characteristic peaks decrease. This may be attributed to the reduction of oleylamine ligand content on the surface of the 0.25 PyMA-CsPbBr$_3$-NC, which confirms that PyMA effectively replaces part of oleylamine molecules and is anchored on the perovskite NC surface. As shown in Fig. 5b, the C–H bond bending vibration peaks representing the PyMA monomer can be observed at 3028 and 2993 cm^{-1}. A less pronounced C–H bond bending vibration peak can also be found at the same position in the 0.25 PyMA-CsPbBr$_3$-NC, but it is absent in the pristine CsPbBr$_3$-NC, strongly supporting that the PyMA ligands have been successfully anchored on the CsPbBr$_3$ NC surface. Fig. 5c and d also reflect similar results. The FT-IR peaks of the PyMA monomer at 1558 and 1600 cm^{-1} belong to the skeleton vibration of the pyridine aromatic ring. Such skeleton vibration peaks were also observed at 1554 and 1610 cm^{-1} in the 0.25 PyMA-CsPbBr$_3$-NC, but there were no such peaks in the pristine CsPbBr$_3$-NC. In the fingerprint area, the out-of-plane deformation vibration of the C–H bond and the deformation vibration peaks of C=C and C=N double bonds were observed in the PyMA monomer,[51] located at 785 and 868 cm^{-1}. Similar FT-IR peaks were also observed at 791 and 869 cm^{-1} in the 0.25 PyMA-CsPbBr$_3$-NC, but such peaks were not detected in the pristine CsPbBr$_3$-NC. Therefore, the above results can intuitively prove that PyMA ligands exist in the PyMA-CsPbBr$_3$-NCs and are also successfully anchored on the perovskite NC surface. Interestingly, from Fig. 5c and d, it can
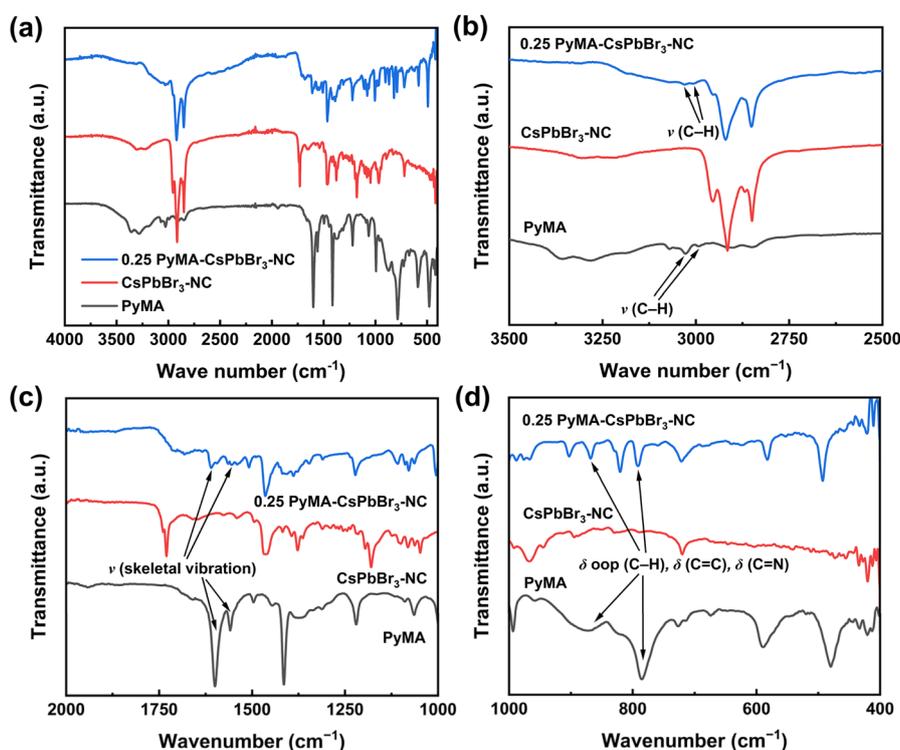

Fig. 5 (a) FT-IR spectra of PyMA, CsPbBr$_3$-NC, and 0.25 PyMA-CsPbBr$_3$-NC. The zoomed-in FT-IR spectra in the (b) 2500–3500 cm^{-1}, (c) 1000–2000 cm^{-1}, and (d) 400–1000 cm^{-1} regions.

be found that the specific FT-IR characteristic peaks in the PyMA monomer are slightly shifted in the 0.25 PyMA-CsPbBr$_3$-NC, and the peak shape has also slightly changed. This may reflect the variations of vibrational mode, vibrational state lifetime, or vibrational mode type at different positions of PyMA ligand binding on the CsPbBr$_3$ cubic lattice.[51]

^{1}H NMR spectroscopy also provided additional evidence for the anchoring of PyMA ligands on the perovskite NC surface. Fig. 6a shows the ^{1}H NMR spectra of the PyMA monomer, CsPbBr$_3$-NC, and 0.25 PyMA-CsPbBr$_3$-NC in deuterated chloroform solution. A doublet peak in the NMR spectrum due to the hydrogen atoms on the pyridine ring can be observed for the PyMA monomer, with a chemical shift of 7.25 ppm. Similarly, in the ^{1}H NMR spectrum of the 0.25 PyMA-CsPbBr$_3$-NC, the doublet peak representing hydrogen on the pyridine ring appears at 7.18 ppm, but this peak has not been found in the pristine CsPbBr$_3$-NC. This indicates that the PyMA ligands have been successfully and efficiently coordinated on the surface of the perovskite NCs. Furthermore, in comparison to the chemical shift of the monomeric PyMA doublet peak, the doublet peak of the 0.25 PyMA-CsPbBr$_3$-NC is shifted towards the upfield. This may be attributed to the fact that PyMA partially replaces the oleylamine molecules anchored on the perovskite surface. The hydrogen atoms on the pyridine ring of PyMA are affected by the electron-donating properties of alkyl ligands near the surrounding space, which enhances the electron cloud density around the hydrogen atoms on the pyridine ring and enables the doublet peak to move upfield.

The effect of PyMA ligands on the surface elements of CsPbBr$_3$ perovskite NCs was investigated by the X-ray photoelectron spectroscopy (XPS) technique. Compared with the pristine CsPbBr$_3$-NC, the N signal of the 0.25 PyMA-CsPbBr$_3$-NC is stronger (Fig. 6b), which may be attributed to the additional PyMA passivating the perovskite surface defects and thereby increasing the –NH$_3^+$ amount. Fig. 6c also shows Pb 4f XPS spectra for the corresponding samples. The pristine CsPbBr$_3$-NC has two obvious XPS characteristic peaks at 137.8 eV and 142.7 eV, which are assigned to 4f$_{7/2}$ and Pb 4f$_{5/2}$, respectively. When PyMA was modified onto the perovskite NCs as a surface ligand, two XPS peaks representing Pb in CsPbBr$_3$ shifted to increased binding energies of 138.2 and 143.1 eV. This suggests that the modification of the perovskite surface using PyMA ligands can effectively passivate the perovskite defects, thereby forming a stronger Pb–Br interaction in the perovskite NC lattice.[52] Fig. 6d shows the XPS spectrum of Cs 3d. The introduction of PyMA has no effect on the binding energy of Cs$^+$, implying that Cs$^+$ on the surface of CsPbBr$_3$ NCs remains in a relatively stable state during the treatment process. By comparing their element contents *via* XPS quantitative analysis, the changes before and after the ligand-exchange process of CsPbBr$_3$ NCs can also be detected, as shown in Fig. 6e and f. After the ligand-exchange process involving aromatic PyMA, the O content decreased and the N content increased, indicating that PyMA with pyridine groups has successfully replaced part of the long-chain oleylamine ligands on the perovskite NC surface. The increase in Cs, Pb, and Br contents compared to the original CsPbBr$_3$-NC indicates that the protonation degree
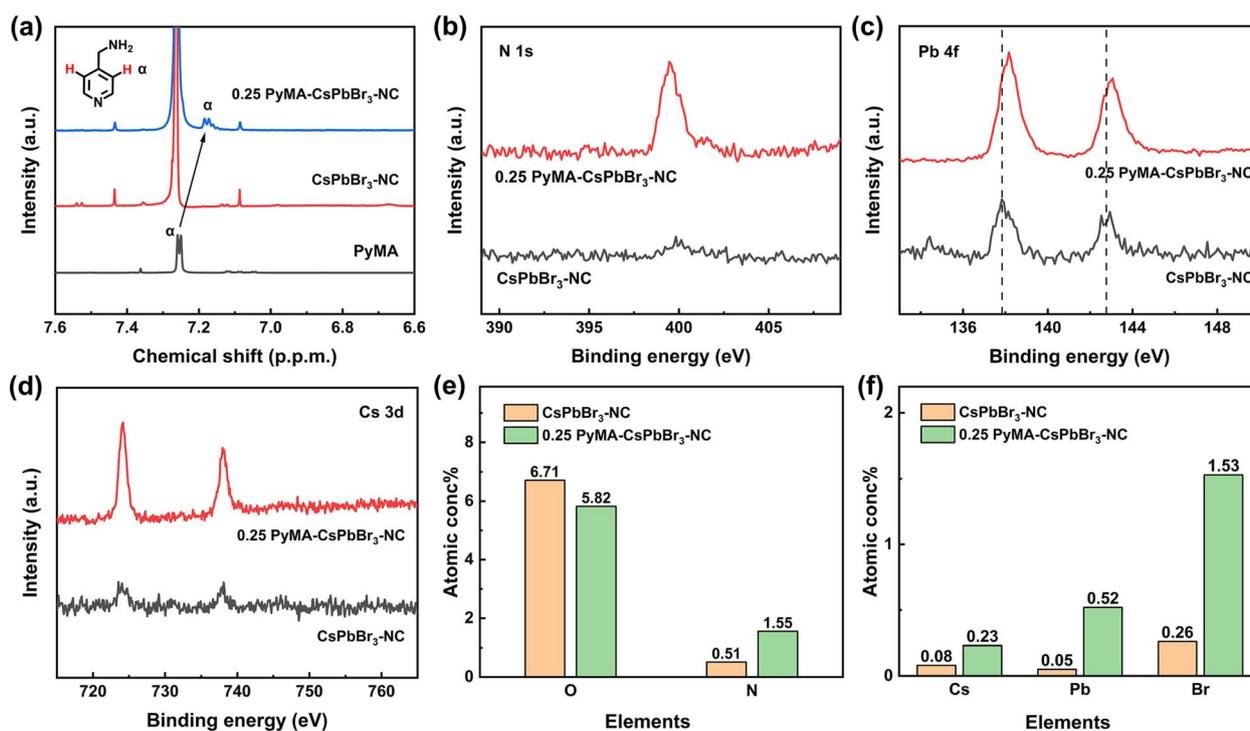

Fig. 6 (a) ^{1}H NMR spectra of PyMA, CsPbBr$_3$-NC, and 0.25 PyMA-CsPbBr$_3$-NC (in CDCl$_3$). XPS spectra of (b) N 1s, (c) Pb 4f, and (d) Cs 3d of the pristine CsPbBr$_3$-NC and 0.25 PyMA-CsPbBr$_3$-NC and their schematic diagrams of the content changes of (e) O and N and (f) Cs, Pb, and Br elements.

of the amine ligand is strengthened following the addition of PyMA, which facilitates the binding of the PyMA ligand to Br^- on the surface of perovskite NCs, thereby reducing surface trap states and promoting the NC growth. Thus, the above characterization tests favorably demonstrate that PyMA, as an effective aromatic surface ligand, can actively participate in the formation of perovskite NCs and promote their excellent growth. Furthermore, the NC stability is also improved, which is beneficial to their optoelectronic performance.

3.5. The NLO absorption properties of porphyrin-pyridyl perovskite NCs

The above analysis demonstrates the successful preparation of PyMA-CsPbBr$_3$-NCs in this work and confirms that the introduction of PyMA can enhance the photophysical performance of perovskite NCs. It is anticipated that this material would display an increased potential in the NLO response. A star-shaped zinc porphyrin trisubstituted triazacoronene compound ZnPr was designed and prepared, which exhibits excellent NLO absorption properties under ultrafast laser irradiation (Fig. S5†). Moreover, studies have shown that molecules containing pyridine groups can form strong coordination interactions with transition metal atoms.[53] We used a CH_2Cl_2 solution of ZnPr–PyMA to explore the potential axial coordination interaction between ZnPr and perovskite NC surface ligands. The CH_2Cl_2 solution of the pure porphyrin molecule ZnPr appears red, as shown in Fig. S6.† When an equimolar amount of PyMA is added, the color changes to brown. The corresponding UV-vis absorption spectra show that the Q band (416 → 424 nm) and Soret band (543 → 556 nm) absorption peaks of the ZnPr solution containing PyMA have undergone obvious redshifts compared to the pure ZnPr solution, which indicates that the pyridine N of PyMA is axially bound to the Zn in ZnPr through coordination interaction.[54]

On this basis, ZnPr was introduced into perovskite NCs. By the axial coordination combination of the Zn element in ZnPr and the PyMA surface ligand in perovskite NCs, the ZnPr-PyMA-CsPbBr$_3$-NC was prepared and its related NLO test was carried out. For comparison, an equal amount of ZnPr was added to the pristine CsPbBr$_3$-NC solution to prepare a ZnPr-CsPbBr$_3$-NC hybrid material. Besides, in order to broaden the NLO application range of perovskite NC hybrid materials, we utilized the PMMA dispersion medium to prepare samples into PMMA films, which can exclude the loss of some nonlinear absorption properties due to nonlinear scattering induced by high-energy laser light under solution conditions.[55] Prior to this, a blank PMMA film was prepared under the same conditions, and its signal was detected through the open-aperture Z-scan, as presented in Fig. S7 and S8.† Under irradiation with 800 and 515 nm fs lasers, its NLO absorption responses are almost negligible, which means that the NLO absorption responses for the samples measured by Z-scan are entirely derived from the samples themselves.[56] The NLO absorption responses of CsPbBr$_3$-NC, ZnPr-CsPbBr$_3$-NC, 0.25 PyMA-CsPbBr$_3$-NC, and ZnPr-0.25 PyMA-CsPbBr$_3$-NC were tested using the standard open-aperture Z-scan technique. The Z-scan signals were

detected at three distinct positions under diverse laser excitations for each sample, as depicted in Fig. S9.† The slight changes in the normalized transmittance at various locations imply excellent homogeneity of the film samples, as well as reliable and consistent NLO performance. Fig. 7a–c and S10† present their corresponding normalized transmittance distributions under 800 nm fs laser excitation with various input pulse energies (56 → 205 nJ). The normalized transmittance of four materials decreased as they approached the focus position, displaying typical reverse saturable absorption (RSA) responses. The as-prepared perovskite NC PMMA films clearly exhibit RSA responses toward the different pulse energies, possessing good experimental robustness.

We extracted and compared the Z-scan curves of different samples under the same incident energy (Fig. 7d); the minimum normalized transmittance (T_{min}) values of CsPbBr$_3$-NC, ZnPr-CsPbBr$_3$-NC, 0.25 PyMA-CsPbBr$_3$-NC, and ZnPr-0.25 PyMA-CsPbBr$_3$-NC are 0.87, 0.84, 0.70, and 0.37, respectively, implying a sequentially decreasing trend, *i.e.*, enhanced RSA performance. By fitting the corresponding Z-scan curves, the relevant nonlinear parameters and their comparisons shown in Fig. 7e, Tables 1 and S1† can be obtained. Compared with the pristine CsPbBr$_3$-NC, the RSA performance of the 0.25 PyMA-CsPbBr$_3$-NC is significantly enhanced, and its β value is 2 times that of the pristine CsPbBr$_3$-NC, highlighting the improved NLO properties of perovskite NCs achieved by the PyMA ligand incorporation. Comparing the T_{min} and β values of the 0.25 PyMA-CsPbBr$_3$-NC and ZnPr-0.25 PyMA-CsPbBr$_3$-NC, it is evident that adding ZnPr porphyrin molecules to the PyMA-modified CsPbBr$_3$ NCs can greatly improve the NLO absorption performance. The β value of the ZnPr-0.25 PyMA-CsPbBr$_3$-NC is nearly 5 times higher than that of the 0.25 PyMA-CsPbBr$_3$-NC. If compared with the original CsPbBr$_3$-NC, the β value of the ZnPr-0.25 PyMA-CsPbBr$_3$-NC hybrid material is increased by an order of magnitude, showing excellent RSA performance.

The above tests demonstrate that by employing the ligand exchange strategy of PyMA and the axial coordination treatment of ZnPr, the NLO absorption properties of perovskite NCs are significantly improved. Therefore, it is necessary to provide a convincing elaboration of the underlying enhancement mechanism. In the light of the NLO theory, third-order NLO processes can be roughly categorized into two types: resonance and non-resonance.[57] The nonlinear absorption process in the resonance region is mainly derived from the actual transition of electrons, which is a linear absorption induced from the ground state to the excited state, and it accounts for a large proportion of the total nonlinear absorption process. The laser photon energy used is typically greater than the bandgap energy of the sample itself so that photons can be excited from the valence band (VB) to the conduction band (CB) more easily. The nonlinear absorption process in the non-resonant region is more derived from virtual transitions and occurs rapidly. In this case, the laser photon energy used is insufficient to excite the electrons for an actual transition to the CB. By converting the UV-vis spectra into the Tauc diagrams, it can be seen that the bandgap values of perovskite NCs are approximately 2.35–2.36 eV (Fig. S11†), which are significantly larger than the photon
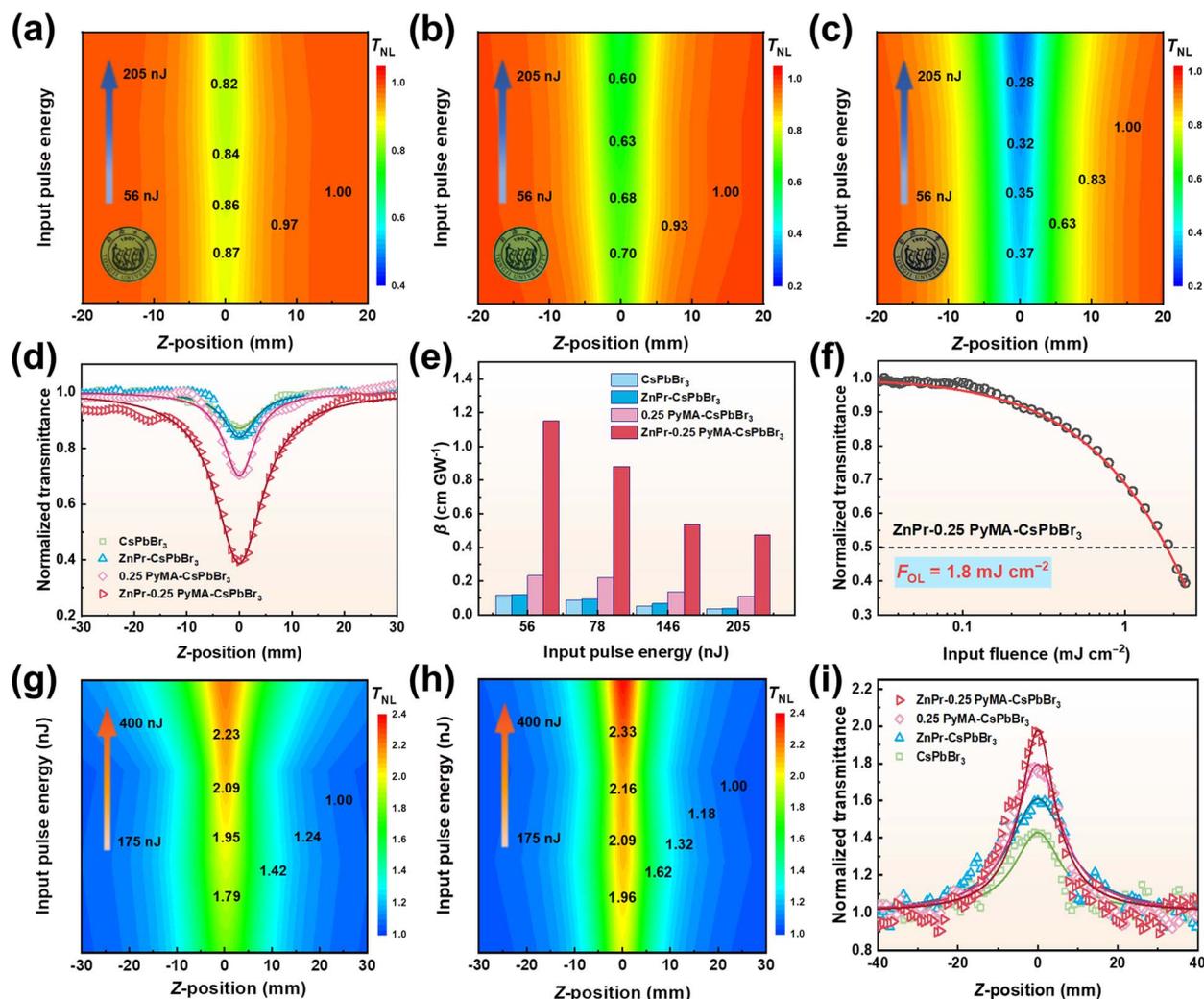
Fig. 7 Normalized transmittance distributions of (a) the pristine $CsPbBr_3$-NC, (b) 0.25 PyMA-$CsPbBr_3$-NC, and (c) ZnPr-0.25 PyMA-$CsPbBr_3$-NC PMMA films under input laser irradiation at 800 nm. Images embedded in the lower-left corner are corresponding photographs. (d) Open-aperture Z-scan traces for all samples under the input energy of 56 nJ at 800 nm. Theoretical fits are indicated by solid lines. (e) The corresponding β values for all samples. (f) Schematic diagram of the relationship between normalized transmittance and input fluence of the ZnPr-0.25 PyMA-$CsPbBr_3$-NC PMMA film. Normalized transmittance distributions of (g) the 0.25 PyMA-$CsPbBr_3$-NC and (h) ZnPr-0.25 PyMA-$CsPbBr_3$-NC PMMA films under input laser irradiation at 515 nm. (i) Open-aperture Z-scan traces for all samples under the input energy of 175 nJ at 515 nm. Theoretical fits are indicated by solid lines.

Table 1 NLO parameters of perovskite NC samples under 800 and 515 nm fs laser irradiation[a]

| Samples | T_{min} | T_{max} | α | | L (μm) | $\beta \times 10^{-3}$ (cm GW^{-1}) |
			800 nm	515 nm		
$CsPbBr_3$	0.87	—	0.02	—	296	117.52 ± 3.33
	—	1.43	—	0.07	—	-96.42 ± 2.26
ZnPr-$CsPbBr_3$	0.84	—	0.07	—	313	119.98 ± 3.87
	—	1.60	—	0.18	—	-115.64 ± 2.24
0.25 PyMA-$CsPbBr_3$	0.70	—	0.16	—	367	231.99 ± 7.06
	—	1.79	—	0.31	—	-129.58 ± 1.26
ZnPr-0.25 PyMA-$CsPbBr_3$	0.37	—	0.08	—	325	1150.47 ± 22.55
	—	1.96	—	0.16	—	-135.81 ± 1.50

[a] T_{max}/T_{min}: maximum/minimum normalized transmittance; α: linear absorbance; L: PMMA film thickness. β: nonlinear absorption coefficient.

energy of the 800 nm fs laser we use, so that actual transitions cannot occur. Interestingly, the bandgap energies of our samples lie between the energy of one photon and that of two photons. Therefore, it is reasonably inferred that under 800 nm fs laser irradiation, our perovskite NC samples undergo a non-resonant two-photon absorption (TPA) process. This inference was also confirmed by power-dependent two-photon PL measurement. Fig. S12† presents the two-photon PL characteristics of our perovskite NC samples under 800 nm fs laser pumping. Their PL intensities continue to increase with the boost of the incident laser power. The corresponding insets depict the relationships between the PL peak intensity and the pump power. On a logarithmic scale, the luminescence intensity shows a linear dependence on the excitation power, with the slope of the fitting curves approximately equal to 2 (following a quadratic power law). These results intuitively demonstrate the TPA mechanism. The TPA performance depends on the influence of the light-induced ground state dipole moment, which is positively correlated with the defect state density originating from the intrinsic states and surface states.[58,59] For the pristine $CsPbBr_3$-NC, the passivation effect of long-chain ligands on defects is weaker than that of the aromatic ligand PyMA, which has been confirmed by the enhanced lifetime of $CsPbBr_3$ NCs after PyMA ligand modification, as reflected in Fig. 4.[60] This leads to an increase in defect state density. Electrons excited from the VB are captured by the trap state and cannot transition to the CB (Fig. 8a), reducing the light-induced ground state dipole moment and thereby resulting in a weak TPA response. In contrast, the partial replacement of long-chain ligands by PyMA effectively passivates surface defects in perovskite, thereby reducing the density of trap states. The improved light-induced ground state dipole moment drives the enhancement of TPA performance. In addition, studies have shown that shorter ligands can induce a stronger electronic coupling effect in adjacent perovskite quantum dots, thereby promoting the enhanced NLO responses of quantum dots.[6,61,62] Through high-resolution TEM (Fig. 2e–h), the quantifiable distances between adjacent NCs of our samples can be estimated. The average distance of the pristine $CsPbBr_3$-NC is 3.23 nm, while the average distances of the $CsPbBr_3$ NCs modified with PyMA contents of 0.075, 0.15, and 0.25 are 2.29, 1.95, and 0.91 nm, respectively. Thus, the introduction of PyMA short-chain aromatic ligands shortens the perovskite lattice spacing, stabilizes the perovskite crystal structure, and promotes the electronic coupling of nanocrystals,[63] resulting in higher NLO absorption responses of PyMA-modified perovskite NCs.

Upon the comparison and analysis of the Z-scan curves and β values for the pristine $CsPbBr_3$-NC and the ZnPr-$CsPbBr_3$-NC control group, it can be found that the nonlinear absorption performance of the ZnPr-$CsPbBr_3$-NC is also boosted after adding porphyrin. This may be because ZnPr, a large planar star-shaped organic molecule with multiple hydrophobic groups, can be adsorbed on the surface of perovskite NCs, which to a certain extent blocks the erosion of the perovskite structure by the external environment and plays a role in enhancing the perovskite stability (Fig. 8b). It was confirmed

from the time-resolved fluorescence spectra of both, as illustrated in Fig. S13,† that the introduction of ZnPr slightly increases the fluorescence lifetime of $CsPbBr_3$ NCs and partially suppresses the non-radiative recombination. Consequently, these factors reduce the density of trap states in perovskite, thus giving this control group material certain nonlinear absorption advantages.

The ZnPr-0.25 PyMA-$CsPbBr_3$-NC hybrid material exhibits a huge NLO response under the 800 nm fs laser irradiation, which may be ascribed to the strong coordination interaction between the Zn atom at the center of the porphyrin ring in ZnPr and the pyridine groups on the ZnPr-0.25 PyMA-$CsPbBr_3$-NC. Although the ZnPr-$CsPbBr_3$-NC in the control group can enhance the NLO performance to a certain extent by adding ZnPr, the inherent insulation of long alkyl chain ligands on the NC surface and the lack of appropriate charge transport pathways between perovskite ligands and porphyrin molecules still restrict the effective charge transfer between porphyrin and perovskite.[47] In contrast, the PyMA ligand with a π-conjugated structure in the ZnPr-0.25 PyMA-$CsPbBr_3$-NC forms the appropriate spatial arrangement on the NC surface, which enhances the electronic coupling between NCs and promotes the improvement of NC conductivity; additionally, the short-chain PyMA aromatic ligand weakens the charge trapping caused by the surface defects of perovskite NCs and reduces their trap state density. More importantly, the pyridine groups on the ZnPr-0.25 PyMA-$CsPbBr_3$-NC interact strongly with the Zn atom at the center of the ZnPr porphyrin ring, allowing porphyrin molecules with macrocyclic planar and hydrophobic groups to be effectively anchored on the surface of $CsPbBr_3$ NCs via PyMA ligands (Fig. 8b). To a greater extent, the NC structure is protected from damage by the external environment, thereby improving the NC stability and ensuring the expression of NLO absorption performance of perovskite itself. The strong coordination also retains many carrier transport channels among $CsPbBr_3$, PyMA ligand, and ZnPr, promoting the charge transport between perovskite NCs and inhibiting non-radiative recombination (Fig. 8b), which is also confirmed by the enhanced fluorescence lifetime of the 0.25 PyMA-$CsPbBr_3$-NC after ZnPr introduction (Fig. S14†). The construction of porphyrin-pyridyl hybrid materials can also make photo-generated carriers bound in the NC inorganic octahedral lattice without being lost due to external losses. Thus, greater exciton binding energy (E_b) is obtained after the interaction with the photoelectric field.[64] This can also be confirmed from the temperature-dependent PL measurement (Fig. S15†). The values of E_b were obtained by fitting the function curves of the integrated intensity of the PL peak vs. temperature using the Arrhenius equation. The results show that the E_b of the pristine $CsPbBr_3$-NC is calculated to be 62.5 meV, while the E_b of 0.25 PyMA-$CsPbBr_3$-NC and ZnPr-0.25 PyMA-$CsPbBr_3$-NC is 71.0 and 74.2 meV, respectively. Hence, these factors synergistically promote the improvement of NLO absorption performance.

It is worth noting that the repair of perovskite defects by PyMA and ZnPr plays a dominant role in enhancing the NLO absorption performance of the entire perovskite NC system. This is because surface defects in NCs are often the main factor
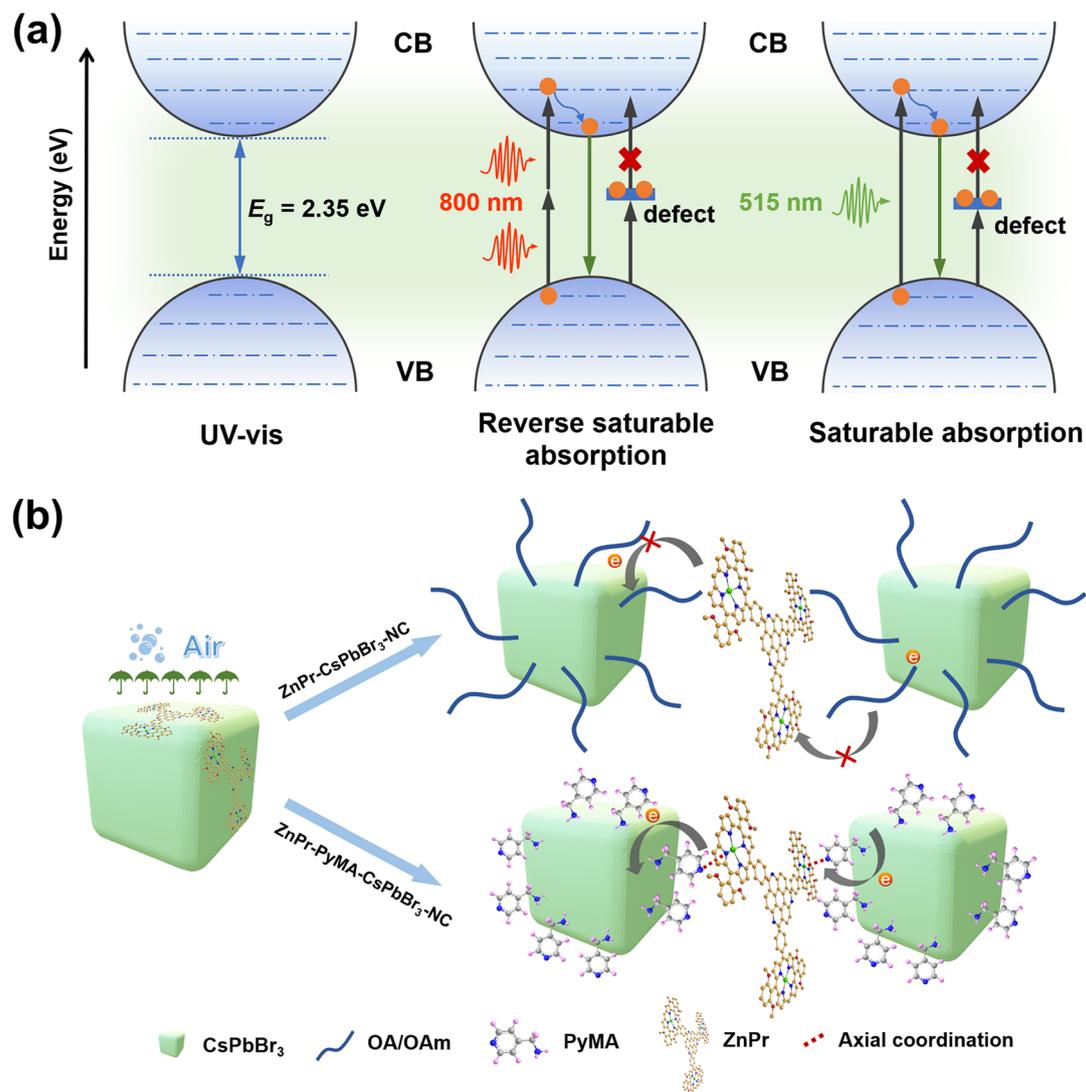
Fig. 8 (a) The proposed NLO absorption mechanism of the perovskite NCs under the ultrafast fs laser irradiation with the wavelengths of 800 and 515 nm. VB: valence band; CB: conduction band. (b) The illustration of the function of ZnPr in carrier transport of the different perovskite NCs (including the pristine and PyMA-treated perovskite NCs).

affecting optical performance. In particular, when their sizes are smaller, the impact of surface defects on the performance is more significant. We use PyMA ligands to anchor on the surface of perovskite NCs to effectively repair perovskite defects, which not only improves the perovskite structure integrity and reduces the trap state density, but also inhibits carrier non-radiative recombination, thereby significantly improving nonlinear absorption coefficients compared to pristine NCs. The introduction of ZnPr, with its large-size plane and hydrophobic properties, can effectively improve the defect passivation effect of PyMA ligands on perovskite NCs through the axial coordination of pyridine N and the porphyrin Zn atom and create environmental barriers against H_2O/O_2 permeation to retain the perovskite inside structure. In essence, it is still to avoid the further generation of defects that would weaken the NLO performance. As for the enhanced exciton binding energy, although it is supported by temperature-dependent PL

measurements (Fig. S15†), its role is secondary to the defect repair mechanism. Moreover, the exciton binding energy is closely related to defects.[65] Too many defect states can also cause excitons to lose energy and reduce exciton stability, resulting in a decrease in their binding energy, which is also evident from the lower E_b of the pristine CsPbBr$_3$-NC (Fig. S15b†). Effective charge transport between components is achieved through the effective coordination of ZnPr and PyMA, which significantly affects the rapid separation and movement of carriers. If the perovskite defect problem cannot be solved, the charge transport pathway will also be disturbed by the defect state.[66] As a result, compared with the defect repair mechanism, an individual charge transport mechanism still has a limited effect on improving the optical absorption nonlinearities.

Since the ZnPr-0.25 PyMA-CsPbBr$_3$-NC hybrid material exhibits excellent RSA properties, its Z-scan curve is converted

into the function relationship between normalized transmittance and input fluence, as shown in Fig. 7f. It can be concluded that the OL threshold (F_{OL}) of the ZnPr-0.25 PyMA-CsPbBr$_3$-NC is 1.8 mJ cm^{-2}, which is better than that of some similar perovskite materials reported, such as CsPbI$_2$Br (F_{OL} = 13.2 mJ cm^{-2})[67] and CsPbBr$_3$ quantum dots (F_{OL} = 10.5–16.9 mJ cm^{-2}).[68] It is also lower than that of some reported quantum dot materials, such as carbon quantum dots (F_{OL} = 74 mJ cm^{-2}).[69] Compared with traditional mature two-dimensional nanomaterials and organic materials, including MoS$_2$ (F_{OL} = 44 mJ cm^{-2}),[70] WSe$_2$ (F_{OL} = 21.6 mJ cm^{-2}),[71] InSe (F_{OL} = 32 mJ cm^{-2}),[72] graphene oxide (F_{OL} = 40 mJ cm^{-2}),[73] organic pyrene derivatives (F_{OL} = 40 mJ cm^{-2}),[74] and organic zwitterion diaminodicyanoquinodimethane (F_{OL} = 117 mJ cm^{-2}),[75] the ZnPr-0.25 PyMA-CsPbBr$_3$-NC prepared in this work still holds an advantage, showing excellent optical limiting performance. These results manifest that the CsPbBr$_3$ perovskite NCs co-processed with ZnPr and PyMA can effectively balance the carrier charge transfer and exciton confinement and improve the overall stability of the hybrid material, thereby synergistically optimizing the NLO absorption performance.

The NLO absorption behaviors of the CsPbBr$_3$-NC, ZnPr-CsPbBr$_3$-NC, 0.25 PyMA-CsPbBr$_3$-NC, and ZnPr-0.25 PyMA-CsPbBr$_3$-NC under 515 nm fs laser irradiation were also studied. Fig. 7g–i and S16† depict their corresponding normalized transmittance distributions with various input pulse energies ranging from 175 to 400 nJ. The normalized transmittance of all samples increases continuously as the sample moves to the focal position, exhibiting obvious saturable absorption (SA) performance. This may be attributed to the fact that the bandgap energies of our prepared perovskite NCs are very close to the excitation photon energy, which can satisfy the excitation conditions within the resonance region. At this point, the probability of electrons transitioning from the VB to the CB is significantly higher than that in the non-resonant region. Therefore, the ground state electrons can easily absorb photons and transition to the excited state to achieve the band-filling state, leading to the SA behavior. We also extracted and compared the Z-scan curves of all samples under the same incident energy, as shown in Fig. 7i. The maximum normalized transmittances (T_{max}) of the four samples are 1.42, 1.60, 1.79, and 1.96, respectively, reflecting the trend of gradually increasing SA intensity. Tables 1 and S2† also give their NLO correlation parameters under SA. Fig. S17 and Table S3† also calculate their ground state (σ_g) and excited state absorption cross-sections (σ_e) by fitting the Z-scan conversion curves with the Frantz-Nodvik model,[76–78] and obtain their ratio (σ_e/σ_g) values. It can be clearly found that the β values of the modified CsPbBr$_3$ NCs are greater than that of the pristine CsPbBr$_3$-NC, while their σ_e/σ_g values of the former are smaller than that of the latter, indicating their excellent SA performance. This is because the introduction of surface ligands and porphyrins enhances the perovskite NC stability. The introduction of PyMA ligands mitigates the electrical insulation caused by long-chain alkyl ligands and diminishes the trap state density on the perovskite NC surface, thereby promoting the electronic coupling between perovskite NCs.[79] Compared to the control

group of ZnPr-CsPbBr$_3$-NC, the SA performance of the ZnPr-0.25 PyMA-CsPbBr$_3$-NC remains superior. This is because ZnPr in the ZnPr-CsPbBr$_3$-NC can be adsorbed on the surface of the CsPbBr$_3$ NC by virtue of its large planar configuration, which improves the structural stability of NC to a certain extent and guarantees the SA expression. However, ZnPr still retains electrical insulation with long-chain alkyl ligands, causing a weak charge transport ability and consequently a diminished SA response. Conversely, the ZnPr-0.25 PyMA-CsPbBr$_3$-NC relies on pyridine ligands to coordinate with Zn atoms on ZnPr, thereby anchoring large planar porphyrin molecules on the perovskite lattice surface from the axial position. The protective ability of ligands is enhanced, the defect sites of perovskite are greatly passivated, and the photogenerated excitons can be tightly bound in the inorganic lattice. These result in a stronger SA response when combined with the optical field. Furthermore, the transport distance between the ligand and perovskite surface becomes shorter, and the coordination interaction effectively enhances the charge transport among porphyrins, PyMA ligands, and perovskite NCs, which jointly enhance the NLO absorption properties of hybrid materials.

This can also be further confirmed by transient absorption (TA) spectroscopy. The fs TA technique with a 520 nm laser as pump light was used to investigate the spectral evolution of 0.25 PyMA-CsPbBr$_3$ and ZnPr-0.25 PyMA-CsPbBr$_3$ NCs in the range of 300–800 nm. The results are displayed as differential transmission ($\Delta T/T$) $vs.$ probe wavelength and delay time (Fig. S18†). The ZnPr-0.25 PyMA-CsPbBr$_3$-NC exhibits a positive transmittance signal in the 540–565 nm probe region centered at 550 nm, which can be attributed to the depletion of the ground state population caused by the electron excitation, $i.e.$ the characteristic of ground state bleaching (GSB).[80,81] And a stimulated emission (SE) signal is shown in the 645–670 nm region. In addition, the sample also exhibits broad negative transmittance signals located in the 565–645 nm and 645–800 nm regions, which is due to the absorption of photoinduced charge carriers from excited states.[82] As the ultrafast relaxation process proceeds (187 ps–1.52 ns), the GSB and ESA signals were obviously detected and exhibited pronounced spectral redshifts, confirming the existence of the ultrafast charge transport process between porphyrins and perovskite NCs.[83,84] To quantify this process, we extracted the GSB kinetics signals of 0.25 PyMA-CsPbBr$_3$ and ZnPr-0.25 PyMA-CsPbBr$_3$ NCs at 556 nm and conducted a temporal analysis of their carrier dynamics. As shown in Fig. S19,† the plotted dynamics clearly illustrates the differences in the relaxation pathways taken by the photogenerated carriers, while the decay rate shows apparent disparity. In the finite relaxation process detection range of 0–2000 ps, the GSB signal of the 0.25 PyMA-CsPbBr$_3$-NC sample decayed rapidly while the ZnPr-0.25 PyMA-CsPbBr$_3$-NC did not decay to a stable state, showing a longer relaxation lifetime. This implies that the band-edge recombination is suppressed due to the competitive charge transport pathways replacing the traditional carrier cooling route in the 0.25 PyMA-CsPbBr$_3$-NC. This can be attributed to the additional pathway generated by the effective charge transport mechanism between porphyrins and perovskite NCs.[85] On the one hand, the excited electrons in the

perovskite NC return to the valence band through intrinsic relaxation; on the other hand, axial coordination between PyMA and ZnPr establishes directional electron transport pathways, which divert carriers from recombination sites, thereby prolonging the relaxation lifetime of the ZnPr-0.25 PyMA-CsPbBr$_3$-NC while suppressing non-radiative losses. Thus, the results indicate that the CsPbBr$_3$ perovskite NC hybrid material after PyMA ligand and ZnPr coordination modifications possesses the best SA performance, implying its huge potential for development in the field of saturable absorbers.

4 Conclusions

In summary, we have proposed an effective strategy to optimize the NLO absorption properties of perovskite NCs and expanded that the NC surface engineering plays an important role in tailoring the NLO responses of perovskites. First, a pyridine-modified CsPbBr$_3$ perovskite NC material was successfully prepared by the ligand-exchange method. Through a series of characterization techniques, such as UV-vis, PL, TRPL, TEM, FTIR, NMR, XPS, *etc.*, the smooth introduction of PyMA aromatic ligands on the perovskite NC surface and the photophysical properties of the materials were verified. Then, taking advantage of the characteristic that the pyridine group is capable of forming the robust coordination interaction with the central metal atom of the porphyrin, the ZnPr porphyrin molecule was incorporated into the PyMA-modified CsPbBr$_3$ perovskite NC to obtain a ZnPr-PyMA-CsPbBr$_3$-NC hybrid material. This hybrid material exhibits enhanced and outstanding NLO absorption properties when exposed to both 800 and 515 nm fs lasers irradiation. In particular, the hybrid material possesses remarkable optical limiting performance, with an OL threshold of 1.8 mJ cm^{-2} upon 800 nm fs laser excitation, which is superior to most of the conventional two-dimensional and organic materials previously reported. The reason is that the introduction of the PyMA ligand and the participation of ZnPr promote the growth of the perovskite crystal structure, lower the trap state density, increase the exciton binding energy, and contribute to the efficient charge transport among the perovskite, surface ligand, and porphyrin. Multiple factors work together to optimize its NLO absorption performance. The strategy reported in our work provides new insights and feasible paradigms for developing multi-domain, broadband ultrafast nonlinear photonic devices based on perovskite NCs.

Data availability

The data that support the findings of this study are available in the ESI† of this article.

Author contributions

Zihao Guan: conceptualization, investigation, major experiments, writing original draft & editing, writing – review & editing. LuLu Fu: writing – review & editing, specifically revision in "Responses to Referees' Comments", nonlinear data analysis

(transient absorption and two-photon photoluminescence). Lu Chen: writing – review & editing, temperature-dependent photoluminescence, morphological measurements. Zhiyuan Wei and Fang Liu: writing – review & editing, Z-scan measurements. Yang Zhao: morphological measurements. Zhipeng Huang: Z-scan fitting analysis. Mark G. Humphrey: writing – review. Chi Zhang: writing – review & editing, supervision.

Conflicts of interest

There are no conflicts to declare.

Acknowledgements

Notes and references

1 M. V. Kovalenko, L. Protesescu and M. I. Bodnarchuk, *Science*, 2017, **358**, 745–750.

2 Y. Xie, B. Peng, I. Bravić, Y. Yu, Y. Dong, R. Liang, Q. Ou, B. Monserrat and S. Zhang, *Adv. Sci.*, 2020, **7**, 2001698.

3 M. F. Lichtenegger, J. Drewniok, A. Bornschlegl, C. Lampe, A. Singldinger, N. A. Henke and A. S. Urban, *ACS Nano*, 2022, **16**, 6317–6324.

4 M. Peng, Y. Ma, L. Zhang, S. Cong, X. Hong, Y. Gu, Y. Kuang, Y. Liu, Z. Wen and X. Sun, *Adv. Funct. Mater.*, 2021, **31**, 2105051.

5 J.-N. Yang, T. Chen, J. Ge, J.-J. Wang, Y.-C. Yin, Y.-F. Lan, X.-C. Ru, Z.-Y. Ma, Q. Zhang and H.-B. Yao, *J. Am. Chem. Soc.*, 2021, **143**, 19928–19937.

6 K. Enomoto, R. Miranti, J. Liu, R. Okano, D. Inoue, D. Kim and Y.-J. Pu, *Chem. Sci.*, 2024, **15**, 13049–13057.

7 C. de Weerd, T. Gregorkiewicz and L. Gomez, *Adv. Opt. Mater.*, 2018, **6**, 1800289.

8 H. Song, J. Yang, W. H. Jeong, J. Lee, T. H. Lee, J. W. Yoon, H. Lee, A. J. Ramadan, R. D. J. Oliver, S. C. Cho, S. G. Lim, J. W. Jang, Z. Yu, J. T. Oh, E. D. Jung, M. H. Song, S. H. Park, J. R. Durrant, H. J. Snaith, S. U. Lee, B. R. Lee and H. Choi, *Adv. Mater.*, 2023, **35**, 2209486.

9 L. Protesescu, S. Yakunin, M. I. Bodnarchuk, F. Krieg, R. Caputo, C. H. Hendon, R. X. Yang, A. Walsh and M. V. Kovalenko, *Nano Lett.*, 2015, **15**, 3692–3696.

10 J.-N. Yang, J.-J. Wang, Y.-C. Yin and H.-B. Yao, *Chem. Soc. Rev.*, 2023, **52**, 5516–5540.

11 S. Das Adhikari, A. F. Gualdrón Reyes, S. Paul, J. Torres, B. Escuder, I. Mora-Seró and S. Masi, *Chem. Sci.*, 2023, **14**, 8984–8999.

12 F. Zhou, Z. Li, H. Chen, Q. Wang, L. Ding and Z. Jin, *Nano Energy*, 2020, **73**, 104757.

13 C. Zhang, J. Chen, L. Kong, L. Wang, S. Wang, W. Chen, R. Mao, L. Turyanska, G. Jia and X. Yang, *Adv. Funct. Mater.*, 2021, **31**, 2100438.

14 T. Zhang, C. Zhou, X. Feng, N. Dong, H. Chen, X. Chen, L. Zhang, J. Lin and J. Wang, *Nat. Commun.*, 2022, **13**, 60.

15 A. K. Dey, S. Das, S. M. Jose, S. Sreedharan, N. Kandoth, S. Barman, A. Patra, A. Das and S. K. Pramanik, *Chem. Sci.*, 2024, **15**, 10935–10944.

16 J. Xu, X. Li, J. Xiong, C. Yuan, S. Semin, T. Rasing and X.-H. Bu, *Adv. Mater.*, 2020, **32**, 1806736.

17 Y. Xu, Q. Chen, C. Zhang, R. Wang, H. Wu, X. Zhang, G. Xing, W. W. Yu, X. Wang, Y. Zhang and M. Xiao, *J. Am. Chem. Soc.*, 2016, **138**, 3761–3768.

18 E. Cassette, T. Mirkovic and G. D. Scholes, *J. Phys. Chem. Lett.*, 2013, **4**, 2091–2093.

19 T. Qiao and D. H. Son, *Acc. Chem. Res.*, 2021, **54**, 1399–1408.

20 J. Bai, L. Wang, T. Zhang, T. Hou, M. Zhang, B. Xu, D. Li, X. Jin, Q. Li, Y. Wang, X. Zhang and Y. Song, *Nano Res.*, 2023, **16**, 1576–1585.

21 Y. Wang, X. Li, X. Zhao, L. Xiao, H. Zeng and H. Sun, *Nano Lett.*, 2016, **16**, 448–453.

22 J. Pan, S. P. Sarmah, B. Murali, I. Dursun, W. Peng, M. R. Parida, J. Liu, L. Sinatra, N. Alyami, C. Zhao, E. Alarousu, T. K. Ng, B. S. Ooi, O. M. Bakr and O. F. Mohammed, *J. Phys. Chem. Lett.*, 2015, **6**, 5027–5033.

23 L. Wang, Y. Zhu, H. Liu, J. Gong, W. Wang, S. Guo, Y. Yu, H. Peng and Y. Liao, *ACS Appl. Mater. Interfaces*, 2019, **11**, 35270–35276.

24 A. F. Gualdrón-Reyes, R. Fernández-Climent, S. Masi, C. A. Mesa, C. Echeverría-Arrondo, F. Aiello, F. Balzano, G. Uccello-Barretta, J. Rodríguez-Pereira, S. Giménez and I. Mora-Seró, *Adv. Opt. Mater.*, 2023, **11**, 2203096.

25 C. Tang, X. Shen, S. Yu, Y. Zhong, Z. Wang, J. Hu, M. Lu, Z. Wu, Y. Zhang, W. W. Yu and X. Bai, *Mater. Today Phys.*, 2021, **21**, 100555.

26 C. Cueto, M. Hu, T. P. Russell and T. Emrick, *J. Am. Chem. Soc.*, 2024, **146**, 8189–8197.

27 G. Li, J. Huang, H. Zhu, Y. Li, J.-X. Tang and Y. Jiang, *Chem. Mater.*, 2018, **30**, 6099–6107.

28 X. Dai, Y. Deng, X. Peng and Y. Jin, *Adv. Mater.*, 2017, **29**, 1607022.

29 J. Dugay, R. P. Tan, M. Ibrahim, C. Garcia, J. Carrey, L. M. Lacroix, P. F. Fazzini, G. Viau and M. Respaud, *Phys. Rev. B: Condens. Matter Mater. Phys.*, 2014, **89**, 041406.

30 E. Zillner, S. Fengler, P. Niyamakom, F. Rauscher, K. Köhler and T. Dittrich, *J. Phys. Chem. C*, 2012, **116**, 16747–16754.

31 M. A. Boles, D. Ling, T. Hyeon and D. V. Talapin, *Nat. Mater.*, 2016, **15**, 141–153.

32 D. S. Dolzhnikov, H. Zhang, J. Jang, J. S. Son, M. G. Panthani, T. Shibata, S. Chattopadhyay and D. V. Talapin, *Science*, 2015, **347**, 425–428.

33 J. H. Park, A.-y. Lee, J. C. Yu, Y. S. Nam, Y. Choi, J. Park and M. H. Song, *ACS Appl. Mater. Interfaces*, 2019, **11**, 8428–8435.

34 H. Zhao, H. Chen, S. Bai, C. Kuang, X. Luo, P. Teng, C. Yin, P. Zeng, L. Hou, Y. Yang, L. Duan, F. Gao and M. Liu, *ACS Energy Lett.*, 2021, **6**, 2395–2403.

35 J. Dai, J. Xi, L. Li, J. Zhao, Y. Shi, W. Zhang, C. Ran, B. Jiao, X. Hou, X. Duan and Z. Wu, *Angew. Chem., Int. Ed.*, 2018, **57**, 5754–5758.

36 N. Xiang, X. Huang, X. Feng, Y. Liu, B. Zhao, L. Deng, P. Shen, J. Fei and S. Tan, *Dyes Pigm.*, 2011, **88**, 75–83.

37 P. Jiang, B. Zhang, Z. Liu and Y. Chen, *Nanoscale*, 2019, **11**, 20449–20455.

38 L. Fu, H. Li, Y. Fang, Z. Guan, Z. Wei, N. Shan, F. Liu, Y. Zhao, M. Zhang, Z. Huang, M. G. Humphrey and C. Zhang, *Nano Res.*, 2023, **16**, 5909–5918.

39 L. Fu, J. Ye, H. Li, Z. Huang, M. G. Humphrey and C. Zhang, *Nano Res.*, 2022, **15**, 1355–1365.

40 Z. Guan, Z. Wei, F. Liu, L. Fu, N. Shan, Y. Zhao, Z. Huang, M. G. Humphrey and C. Zhang, *ACS Appl. Mater. Interfaces*, 2023, **15**, 51626–51638.

41 H. Lv, X.-P. Zhang, K. Guo, J. Han, H. Guo, H. Lei, X. Li, W. Zhang, U.-P. Apfel and R. Cao, *Angew. Chem., Int. Ed.*, 2023, **62**, e202305938.

42 C. F. A. Negre, R. L. Milot, L. A. Martini, W. Ding, R. H. Crabtree, C. A. Schmuttenmaer and V. S. Batista, *J. Phys. Chem. C*, 2013, **117**, 24462–24470.

43 H. Xia, M. Zhang, H. Wang, Y. Sun, Z. Li, R. Ma, H. Liu, T. A. Dela Peña, H. T. Chandran, M. Li, J. Wu, X. Lu, W.-Y. Wong and G. Li, *Adv. Funct. Mater.*, 2024, 2411058.

44 M. Sheik-Bahae, A. A. Said, T. H. Wei, D. J. Hagan and E. W. V. Stryland, *IEEE J. Quantum Electron.*, 1990, **26**, 760–769.

45 A. Pramanik, S. Patibandla, Y. Gao, K. Gates and P. C. Ray, *JACS Au*, 2021, **1**, 53–65.

46 F. Bertolotti, L. Protesescu, M. V. Kovalenko, S. Yakunin, A. Cervellino, S. J. L. Billinge, M. W. Terban, J. S. Pedersen, N. Masciocchi and A. Guagliardi, *ACS Nano*, 2017, **11**, 3819–3831.

47 M. Yu, D. Zhang, Y. Xu, J. Lin, C. Yu, Y. Fang, Z. Liu, Z. Guo, C. Tang and Y. Huang, *J. Colloid Interface Sci.*, 2022, **608**, 2367–2376.

48 T. Zhang, M. Long, L. Pan, K. Ngai, M. Qin, F. Xie, X. Lu, J. Chen and J. Xu, *Sci. Bull.*, 2020, **65**, 1832–1839.

49 H. Wu, Z. Kang, Z. Zhang, H. Si, S. Zhang, Z. Zhang, Q. Liao and Y. Zhang, *Small Methods*, 2019, **3**, 1900117.

50 Y.-H. Kim, C. Wolf, Y.-T. Kim, H. Cho, W. Kwon, S. Do, A. Sadhanala, C. G. Park, S.-W. Rhee, S. H. Im, R. H. Friend and T.-W. Lee, *ACS Nano*, 2017, **11**, 6586–6593.

51 E. Pretsch, P. Bühlmann and M. Badertscher, in *Structure Determination of Organic Compounds: Tables of Spectral Data*, Springer Berlin Heidelberg, Berlin, Heidelberg, 2009, pp. 1–67, DOI: 10.1007/978-3-540-93810-1_7.

52 S. Wang, Y. Wang, Y. Zhang, X. Zhang, X. Shen, X. Zhuang, P. Lu, W. W. Yu, S. V. Kershaw and A. L. Rogach, *J. Phys. Chem. Lett.*, 2019, **10**, 90–96.

53 R. Dobrawa and F. Würthner, *J. Polym. Sci., Part A: Polym. Chem.*, 2005, **43**, 4981–4995.

54 L. A. Martini, G. F. Moore, R. L. Milot, L. Z. Cai, S. W. Sheehan, C. A. Schmuttenmaer, G. W. Brudvig and R. H. Crabtree, *J. Phys. Chem. C*, 2013, **117**, 14526–14533.

55 S. Zhu, Q. Zhang, Q. Pan, J. Hu, R. Liu, G. Song and H. Zhu, *Appl. Surf. Sci.*, 2022, **584**, 152567.

56 J. Huang, F. Lang, Y. Cui, L. Xie, K. Geng, Y. Zhao and H. Hou, *Adv. Opt. Mater.*, 2022, **10**, 2201872.

57 B. S. Kalanoor, L. Gouda, R. Gottesman, S. Tirosh, E. Haltzi, A. Zaban and Y. R. Tischler, *ACS Photonics*, 2016, **3**, 361–370.

58 B.-H. Zhu, H.-C. Zhang, Z.-Y. Zhang, Y.-P. Cui and J.-Y. Zhang, *Appl. Phys. Lett.*, 2011, **99**, 231903.

59 B. H. Zhu, H. C. Zhang, J. Y. Zhang, Y. P. Cui and Z. Q. Zhou, *Appl. Phys. Lett.*, 2011, **99**, 021908.

60 G. Li, J. Huang, Y. Li, J. Tang and Y. Jiang, *Nano Res.*, 2019, **12**, 109–114.

61 H. Tahara, M. Sakamoto, T. Teranishi and Y. Kanemitsu, *Nat. Nanotechnol.*, 2024, **19**, 744–750.

62 G. Rodary, L. Bernardi, C. David, B. Fain, A. Lemaître and J.-C. Girard, *Nano Lett.*, 2019, **19**, 3699–3706.

63 K. Enomoto, R. Miranti, J. Liu, R. Okano, D. Inoue, D. Kim and Y.-J. Pu, *Chem. Sci.*, 2024, **15**, 13049–13057.

64 Z. Guan, L. Fu, Z. Wei, N. Shan, H. Li, Y. Fang, Y. Zhao, Z. Huang, M. G. Humphrey and C. Zhang, *Mater. Today Phys.*, 2023, **35**, 101135.

65 D. Liu, C. Zhang, J. Shi, Y. Shi, T. T. T. Nga, M. Liu, S. Shen and C.-L. Dong, *Small*, 2024, **20**, 2310289.

66 A. Musiienko, D. R. Ceratti, J. Pipek, M. Brynza, H. Elhadidy, E. Belas, M. Betušiak, G. Delport and P. Praus, *Adv. Funct. Mater.*, 2021, **31**, 2104467.

67 K. S. Rao, R. A. Ganeev, K. Zhang, Y. Fu, G. S. Boltaev, S. K. Maurya and C. Guo, *Opt. Mater.*, 2019, **92**, 366–372.

68 C. Zhu, L. Wang, D. Zhao, Y. Yang, X. Liu, B. Xu, Z. Xu and J. Qiu, *Opt. Lett.*, 2021, **46**, 5216–5219.

69 D. Tan, Y. Yamada, S. Zhou, Y. Shimotsuma, K. Miura and J. Qiu, *Carbon*, 2014, **69**, 638–640.

70 R. Wei, H. Zhang, X. He, Z. Hu, X. Tian, Q. Xiao, Z. Chen and J. Qiu, *Opt. Mater. Express*, 2015, **5**, 1807–1814.

71 X. Tian, R. Wei, Q. Guo, Y. J. Zhao and J. Qiu, *Adv. Mater.*, 2018, **30**, e1801638.

72 X. Yan, X. Wu, Y. Fang, W. Sun, C. Yao, Y. Wang, X. Zhang and Y. Song, *Opt. Mater.*, 2020, **108**, 110171.

73 X.-F. Jiang, L. Polavarapu, H. Zhu, R. Ma and Q.-H. Xu, *Photonics Res.*, 2015, **3**, A87–A91.

74 A. Husain, A. Ganesan, M. Sebastian and S. Makhseed, *Dyes Pigm.*, 2021, **184**, 108787.

75 A. Patra, N. Venkatram, D. N. Rao and T. P. Radhakrishnan, *J. Phys. Chem. C*, 2008, **112**, 16269–16274.

76 J. Huang, N. Dong, S. Zhang, Z. Sun, W. Zhang and J. Wang, *ACS Photonics*, 2017, **4**, 3063–3070.

77 S. Zhang, Y. Li, X. Zhang, N. Dong, K. Wang, D. Hanlon, J. N. Coleman, L. Zhang and J. Wang, *Nanoscale*, 2016, **8**, 17374–17382.

78 H. Chen, L. Gao, O. A. Al-Hartomy, F. Zhang, A. Al-Ghamdi, J. Guo, Y. Song, Z. Wang, H. Algarni, C. Wang, S. Wageh, S. Xu and H. Zhang, *Nanoscale*, 2021, **13**, 15891–15898.

79 X. Liu, H. Zhao, L. Wei, X. Ren, X. Zhang, F. Li, P. Zeng and M. Liu, *Nanophotonics*, 2020, **10**, 1967–1975.

80 Q. Li and T. Lian, *J. Phys. Chem. Lett.*, 2019, **10**, 566–573.

81 B. R. C. Vale, E. Socie, A. Burgos-Caminal, J. Bettini, M. A. Schiavon and J.-E. Moser, *J. Phys. Chem. Lett.*, 2020, **11**, 387–394.

82 K. Justice Babu, G. Kaur, A. Shukla, A. Kaur, T. Goswami, N. Ghorai and H. N. Ghosh, *J. Phys. Chem. Lett.*, 2021, **12**, 302–309.

83 A. N. Yadav, A. K. Singh, S. Srivastava, M. Kumar, B. K. Gupta and K. Singh, *Phys. Chem. Chem. Phys.*, 2019, **21**, 6265–6273.

84 C.-H. Chuang, T. L. Doane, S. S. Lo, G. D. Scholes and C. Burda, *ACS Nano*, 2011, **5**, 6016–6024.

85 J. Zhang, B. Zhu, L. Zhang and J. Yu, *Chem. Commun.*, 2023, **59**, 688–699.